

Gate-tunable strong spin-orbit interaction in two-dimensional tellurium probed by weak antilocalization

Chang Niu,^{1,2} Gang Qiu^{1,2}, Yixiu Wang,³ Zhuocheng Zhang^{1,2}, Mengwei Si,^{1,2} Wenzhuo Wu,³ and Peide D. Ye^{1,2,*}

¹*School of Electrical and Computer Engineering, Purdue University, West Lafayette, Indiana 47907, USA*

²*Birck Nanotechnology Center, Purdue University, West Lafayette, Indiana 47907, USA*

³*School of Industrial Engineering, Purdue University, West Lafayette, Indiana 47907, USA*



(Received 19 December 2019; accepted 1 April 2020; published 12 May 2020)

Tellurium (Te) has attracted great research interest due to its unique crystal structure since the 1970s. However, the conduction band of Te is rarely studied experimentally because of the *p*-type accumulation layer at the surface of Te. By the atomic layer deposited dielectric doping technique, we are able to access the conduction-band transport properties of Te in a controlled fashion. In this paper, we report on a systematic study of the weak-anti-localization (WAL) effect in *n*-type two-dimensional (2D) Te films. We find that WAL agrees well with Iordanskii, Lyanda-Geller, and Pikus theory. The gate and temperature-dependent WAL reveal that the D'yakonov-Perel mechanism, dominant for spin relaxation and phase relaxation, is governed by electron-electron interaction. A large phase-coherence length near 600 nm at $T = 1$ K is obtained together with gate-tunable spin-orbit interaction (SOI). Transition from weak-localization to WAL depending on gate bias is also observed. These results demonstrate that newly developed solution-based synthesized Te films provide a new controllable strong SOI 2D semiconductor with high potential for spintronic applications.

DOI: [10.1103/PhysRevB.101.205414](https://doi.org/10.1103/PhysRevB.101.205414)

Spin-orbit interaction (SOI) in two-dimensional (2D) materials brings many exotic phenomena to be explored. In transition-metal dichalcogenides, large SOI-induced band splitting in both conduction and valence bands gives rise to the valley Hall effect [1,2] and the unconventional quantum Hall effect [3,4]. Recently, band inversion caused by the spin-orbit coupling proximity effect [5] is observed in the graphene/WS₂ heterostructure [6]. SOI has been extensively studied in III-V semiconductors, such as InGaAs/InAlAs quantum wells for spintronic applications [7–9]. Chiral crystals with SOI are predicted to host Kramers-Weyl fermions and other topological quantum properties [10].

Weak-antilocalization (WAL) and weak localization (WL) caused by the interference of two time-reversal electron wave paths when electrons are scattered by impurities are used to probe SOI in conventional semiconductors [11] and now to be extended to 2D materials research, such as graphene [12,13], MoS₂ [14,15], black phosphorus [16–19], and others [20–23]. A correction to magnetoconductance due to the backscattered constructive or destructive interference between electrons is sensitive to the phase coherence and spin relaxation of electrons. WAL is also found in topologically nontrivial systems, such as topological insulators [24,25], Dirac [26], and Weyl [27] semimetals due to the significant Berry's phase.

Tellurium (Te) is a narrow band-gap (0.35-eV) semiconductor with a hexagonal crystal structure formed by van der Waals interaction between each one-dimensional helical atom chain. Covalently bonded atoms rotate around the *c* axis in a period of three atoms as shown in Fig. 1(a). The valence band

and conduction band are located in the corner of Brillouin zone *H* and *H'* points [Fig. 1(b)]. Theoretically, Te is predicted to undergo transformation into a topological insulator under strain [28] and a Weyl semimetal under pressure [29]. Te has a *p*-type accumulation layer at the surface [30], therefore, up to date, most of the experiments including thermoelectric properties [31], quantum Hall effect [32], and angle-resolved photoemission spectroscopy [33] were performed in *p*-type Te samples. The lack of inversion symmetry and the strong spin-orbit coupling of Te give rise to the camelbacklike structure in the valence band [32] and Rashba-like spin splitting bands with nontrivial radial spin texture in the conduction band [29,34]. The spin-split conduction bands cross at the *H* point and form a Weyl point protected by the threefold screw symmetry of the helical crystal [28]. The spin-orbit interaction and its mechanism in *n*-type Te is explored here.

In this paper, we perform magnetotransport measurements of 2D *n*-type Te at cryogenic temperatures. WAL is observed at low magnetic fields less than 0.2 T. Temperature and gate-dependent WAL are systematically measured and analyzed. The spin-relaxation and phase-relaxation mechanisms are studied, showing the high quality of the 2D Te film and the existing strong SOI in this material.

The inset of Fig. 1(c) is an optical image of a Te device with a Hall-bar structure for magnetotransport studies. Source and drain electrodes were made along the long edge of the flake which coincides with the direction of the atomic chains [35]. Hall bars are used to measure the longitudinal and transverse resistances with the backgate to tune the film electron density. The sketch of a typical *n*-type field-effect device is shown in Fig. 1(d). The 20-nm Al₂O₃ is grown by atomic layer deposition at 200 °C to dope tellurium into *n* type [36,37]. A similar effect has also been observed in black phosphorus

*Author to whom correspondence should be addressed: yep@purdue.edu

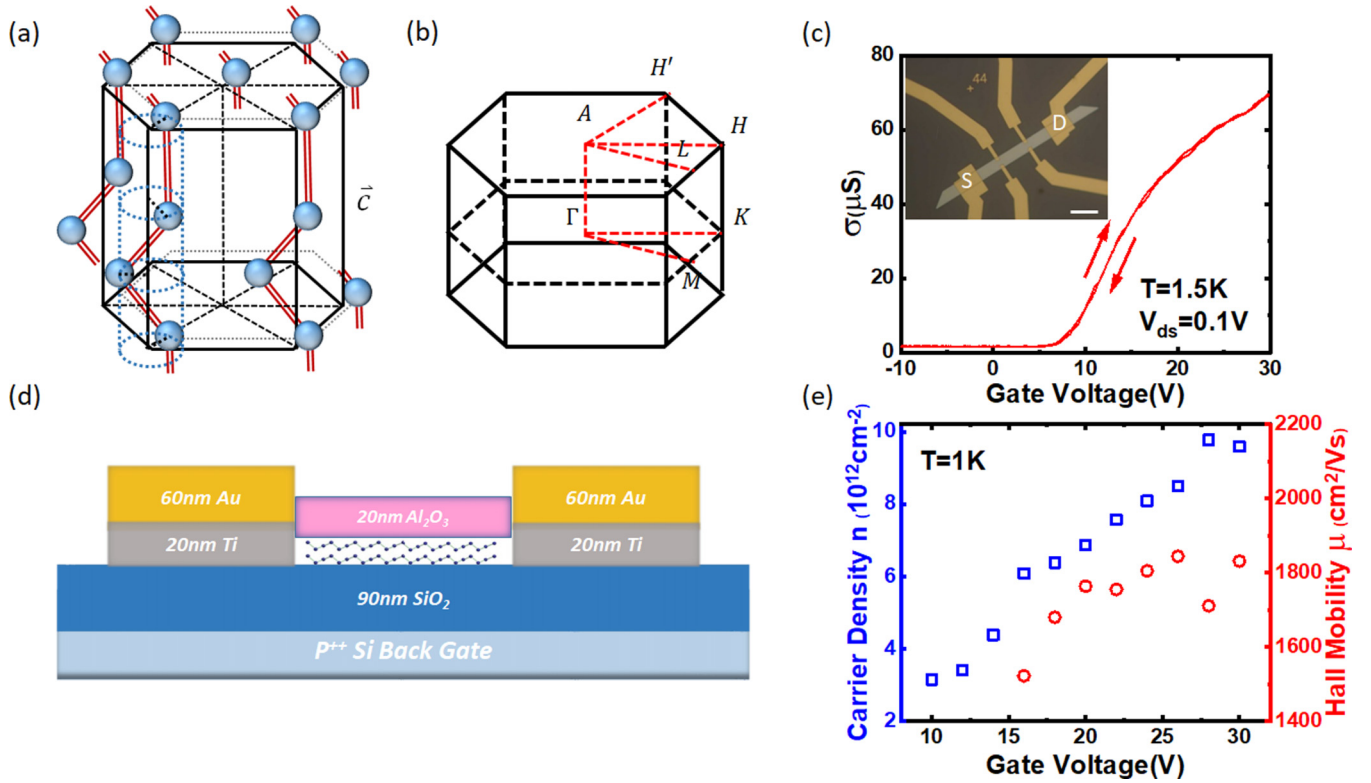


FIG. 1. (a) Crystal structure of Te. Te has one-dimensional helical atom chains along the \vec{c} direction and the hexagonal structure is formed by van der Waals interaction between each chain. (b) The first Brillouin zone of Te. The Te conduction-band minima are located in H and H' points. (c) Transfer curve of a n -type Te field-effect device with a Te film thickness of 10 nm at 1.5 K. The inset: An optical image of a Hall-bar device for transport measurement with helical atom chains (c axis) along the long edge of the flake. The scale bar is 20 μm . (d) Device structure sketch of a n -type Te field-effect transistor. (e) Gate-dependent carrier density n (blue squares, left axis) and electron mobility μ (red circles, right axis) extracted from the Hall measurement at 1 K.

[38,39]. Tellurium flakes with thicknesses around 10 nm are transferred onto a 90-nm SiO_2/Si substrate, which served as a backgate for the transistor, and 20-nm Ti /60-nm Au are used for n -type contact. In order to prove the n -type doping effect, a transfer curve of a Te field-effect device is measured [Fig. 1(c)] using a four-terminal method. By carrying out the Hall measurement, we can calculate the two-dimensional carrier density n and electron Hall mobility μ under different gate biases [Fig. 1(e)] using $n = \frac{1}{e} \left(\frac{dB_{xy}}{dR_{xx}} \right)$ and $\mu = \left(\frac{L}{W} \right) \left(\frac{1}{R_{xx} n e} \right)$, where L is the channel length, W is the channel width, R_{xx} is the longitudinal resistance, and R_{xy} is the Hall resistance. More than ten devices were fabricated and measured, all of which show similar and reproducible behaviors. All the results presented below are from one representative device. Another n -type Te WAL device is analyzed in the Supplemental Material [40]. WAL is also measured and analyzed in undoped intrinsic p -type 2D Te films with gate and temperature dependence as shown in the Supplemental Material [40].

Two different spin-relaxation mechanisms can be used to explain the formation of WAL: the D'yakonov-Perel (DP) and the Elliot-Yafet (EY) spin-relaxation mechanisms [41]. The EY spin-relaxation mechanism often exists in spin degenerated bands in which spin-up and spin-down states are entangled by SOI. When an elastic-scattering (momentum-scattering) process occurs, the electron spin may flip during the scattering. The DP spin relaxation is attributed to the

spin-precession process caused by an effective magnetic-field B_{eff} ($B_{\text{eff}} \propto \vec{E} \times \vec{p}$ [42,43] where \vec{E} is the electric field and \vec{p} is the electron momentum) which is induced by Rashba [44] and/or Dresselhaus SOI [45]. The electron spin makes the precession along the effective magnetic-field direction during the elastic-scattering process. The scattering of an electron by impurities and phonons which changes the electron momentum \vec{p} , fluctuate the effective magnetic-field B_{eff} and suppress the spin relaxation. Therefore, the spin-relaxation time τ_{so} is proportional to the momentum-scattering time τ_{tr} for the EY spin-relaxation mechanism and inversely proportional to τ_{tr} for the DP mechanism [21,46]. Rashba SOI induced by the external electric field and Dresselhaus SOI induced by crystal electric field in inversion asymmetric materials contribute to band spin splitting even at zero external magnetic field.

WAL based on the EY spin-relaxation mechanism is described by the Hikami, Larkin, and Nagaoka (HLN) theory [47], meanwhile, the Iordanskii, Lyanda-Geller, and Pikus (ILP) [48] theory is based on the DP mechanism. Both theories are valid when the external magnetic-field B is smaller than the characteristic magnetic field for transport B_{tr} ($B_{tr} = \hbar/4eD\tau_{tr}$ where D is the diffusion constant and τ_{tr} is the momentum-scattering time). B_{tr} in n -type Te is determined to be 0.2 T in the Supplemental Material [40]. All the results in this paper are from the fitting of data below 0.2 T. Zero-field conductivity is calculated to be much larger than $\frac{e^2}{h}$, therefore,

the effect of small conductivity on weak localization [49] is not considered in this paper. Fittings of Te WAL experimental data with both theories are shown in Fig. 2 where the red line presents for ILP theory and the blue line presents for HLN theory in the Supplemental Material [40]. It is clear that the

ILP fitting provides better agreement with experimental data, indicating that the DP spin-relaxation mechanism is dominant in Te single-crystal films.

Magnetoconductance of WAL using ILP theory is expressed as shown below [41,46],

$$\begin{aligned} \sigma_{xx}(B) - \sigma_{xx}(0) &= \frac{e^2}{2\pi^2\hbar} \left\{ \Psi\left(\frac{1}{2} + \frac{B_\varphi}{B} + \frac{B_{so}}{B}\right) - \ln \frac{B_\varphi + B_{so}}{B} + \frac{1}{2} \Psi\left(\frac{1}{2} + \frac{B_\varphi}{B} + \frac{2B_{so}}{B}\right) - \frac{1}{2} \ln \frac{B_\varphi + 2B_{so}}{B} \right. \\ &\quad \left. - \frac{1}{2} \Psi\left(\frac{1}{2} + \frac{B_\varphi}{B}\right) + \frac{1}{2} \ln \frac{B_\varphi}{B} \right\} \\ B_x &= \frac{\hbar}{4eD\tau_x}, \quad L_x = \sqrt{D\tau_x}, \quad x = so, \varphi, \quad B_{so} = \frac{\hbar}{4eD} |\Omega_3|^2 \tau_{tr}, \end{aligned} \quad (1)$$

where e is the elementary charge, \hbar is the reduced Planck constant, ψ is the function, D is the diffusion constant, τ_φ is the phase-relaxation time, τ_{so} is the spin-relaxation time, Ω_3 is the k -cubic-dependent spin-precession vector, L_{so} and L_φ are the spin-relaxation length and phase-coherence length, respectively. B_φ and B_{so} are the only two fitting parameters. From the ILP fitting in the Supplemental Material [40], we conclude that the k -linear SOI effect is much smaller than the k -cubic SOI effect in our Te sample which is different from III-V semiconductors because, according to Fig. S2 in the Supplemental Material [40], the fittings are good when the k -linear term is small. The intervalley scattering is also considered in the Supplemental Material [40].

In order to extract τ_{so} from B_{so} , the diffusion constant D ($D = v_F^2 \tau_{tr}/2$, where v_F is the Fermi velocity) and the effective mass m^* are calculated from Hall measurement and temperature-dependent Shubnikov-de Haas oscillations in the Supplemental Material [40]. We are able to extract the effective mass of electrons $m_e^* = 0.11m_0$, where m_0 is the bare electron mass (see Fig. S1 in the Supplemental Material [40]). This is consistent with the previous theoretical prediction [50]. The Te conduction-band minimum is at the H point of the Brillouin zone [Fig. 1(b)] which has twofold valley degeneracy and twofold spin degeneracy [29]. To better

understand the spin-relaxation mechanism in Te, the density dependence of WAL is measured and analyzed [Fig. 3(a)]. The relation between spin-relaxation time τ_{so} and momentum-scattering rate τ_{tr}^{-1} [40] is presented in Fig. 3(b). The red eye guideline indicates that τ_{so} is inversely proportional to τ_{tr} . This result together with the better fitting of experimental data with ILP theory unveils that DP spin-relaxation mechanism (spin precession) is dominant in n -type 2D Te films.

$B_\varphi(L_\varphi)$ and $B_{so}(L_{so})$ are extracted from WAL curves [Figs. 3(c) and 3(d)]. The phase-coherence length L_φ reaches as high as 573 nm at $V_{bg} = 30$ V which is larger than that of p -type Te [51] (Fig. S9c of the Supplemental Material [40]) and other 2D materials [14,15,20–22,43,51–54]. It is worth mentioning that the elastic-scattering length is extracted to be L_e (23–47 nm) which is one order of magnitude smaller than the phase-coherence length in all gate voltages. Thus, the electron transport in n -type Te at low temperatures is in the quantum diffusive regime. In addition, the decrease in spin-relaxation length L_{so} with the gate voltage can only be explained by the decrease in τ_{so} (stronger SOI) at a higher gate voltage because D is increasing with gate voltage according to $L_{so} = \sqrt{D\tau_{so}}$ and $D = v_F^2 \tau_{tr}/2$. This further confirms that spin splitting can be tuned by the gate in n -type Te. The gate-tunable SOI together with the long phase-coherence length gives 2D Te a new edge for spintronic applications over other 2D materials that either lack controllable SOI (such as graphene [12,13]) or suffer from short phase-coherence length. The phase-coherence length L_φ increases with back-gate-voltage V_{bg} , implying that electron-electron (e-e) scattering is the main phase-relaxation mechanism. We will further discuss the dephasing mechanism below, which plays an important role in the formation of WAL.

Both Rashba and Dresselhaus SOI have k -cubic-dependent spin-precession vector Ω_3 [44] and the strength are increasing with carrier density, thus, Fermi vector. However, the strength of the Rashba term is also controlled by the external electric field (induced by gate voltage). Here, the relation between Ω_3 and k_F^3 (extracted from B_{so} and carrier density n) are plotted in Fig. 4. Linear fitting of the data (red solid line) shows a change at $V_{bg} = 16$ V ($D = 0.69$ V/nm) which indicates that both Rashba and Dresselhaus SOIs exist in n -type Te and the Rashba effect occurs after the displacement field is larger than $D = 0.69$ V/nm. We estimate the spin-splitting energy is approximately 2.6–8 meV from $2\Delta = 2\hbar|\Omega_3|$ [44].

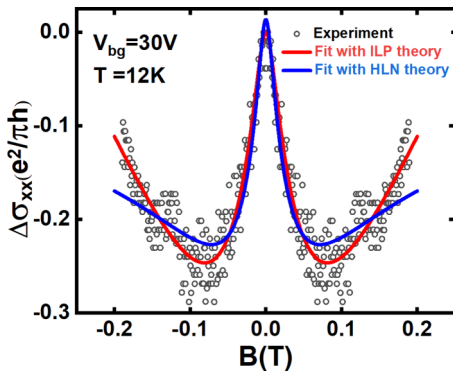


FIG. 2. Experimental WAL data (black circles) measured at $T = 12$ K $V_{bg} = 30$ V and fitting curves with different theories (red line for the ILP theory, blue line for the HLN theory). The IPL theory (red line) provides better agreement with experimental data. Zero-field conductivity is calculated ($\sigma_{xx} = 228.8 e^2/\pi h$).

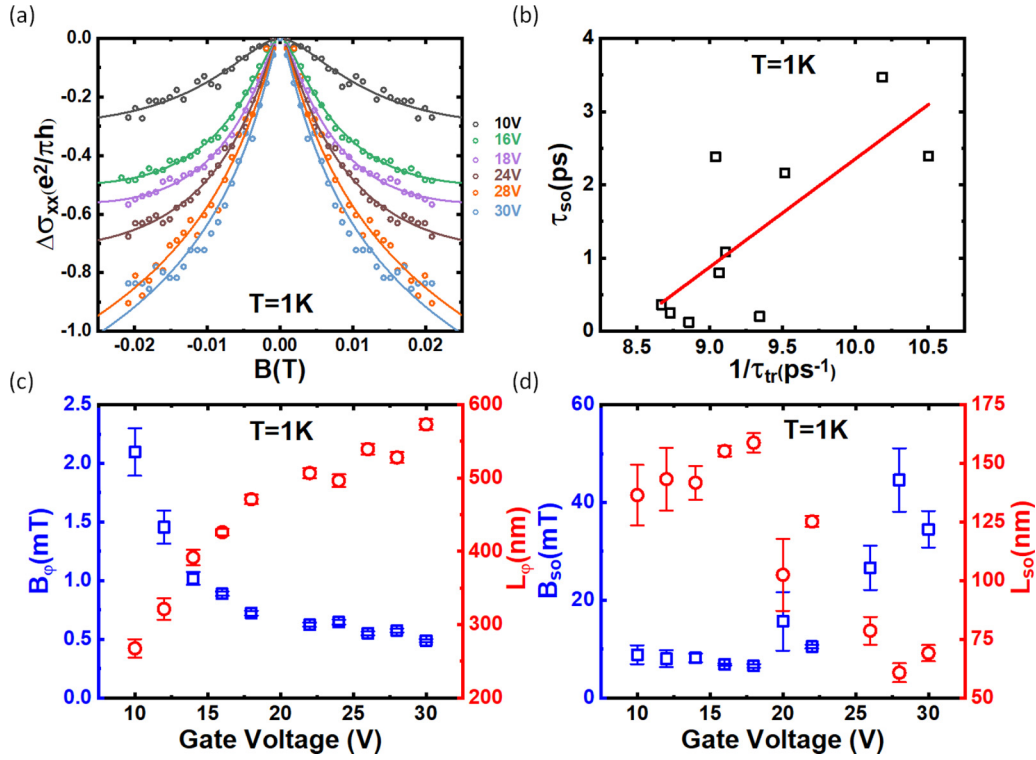


FIG. 3. Gate dependence of WAL. (a) Theoretical fits (solid lines) with ILP theory to experimental data (circles) measured at various backgate voltages. Zero-field conductivity is calculated ($\sigma_{xx} = 64.1 - 227.9 e^2/\pi h$). (b) Spin-relaxation time τ_{so} as a function of momentum-scattering rate τ_{tr}^{-1} at $T = 1$ K. The red solid line is the linear fit of data points. The positive correlation between τ_{so} and τ_{tr}^{-1} indicates the DP spin-relaxation mechanism is dominant in Te. (c) Gate-dependent B_ϕ (blue squares, left axis) and phase-coherence length L_ϕ (red circles, right axis) extracted from the WAL fitting at $T = 1$ K. (d) Gate-dependent B_{so} (blue squares, left axis) and spin-relaxation length L_{so} (red circles, right axis) extracted from the WAL fitting at $T = 1$ K.

In general, phase-coherence length is limited by inelastic electron-electron scattering and electron-phonon (e-ph) scattering [20]. For inelastic electron-electron scattering with small energy transfer, phase-coherence length L_ϕ is expressed as [17]

$$L_\phi = \frac{\hbar^2 \sigma_{xx}}{\pi e^2} \left(m^* k_B T \ln \frac{\sigma_{xx} \hbar}{e^2} \right)^{-1/2}, \quad (2)$$

by the Altshuler-Aronov-Khmelnitsky (AAK) theory [55]. To further investigate the inelastic-scattering mechanism of Te,

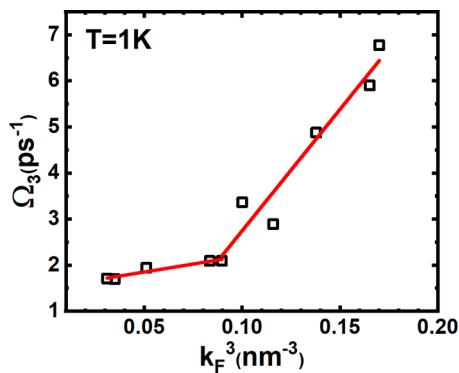


FIG. 4. The relation between k -cubic spin-precession vector Ω_3 and Fermi vector k_F^3 . Two stages are shown in the plot (red solid lines): the change in the slope means that the Rashba effect is strong after $V_{bg} = 16$ V ($D = 0.69$ V/nm).

temperature-dependent WAL is also measured as shown in Fig. 5(a). When the temperature increases, WAL peaks attenuate because of the decrease in the phase-coherence length [Fig. 5(b)]. The temperature-dependent phase-coherence length $L_\phi \propto T^{-\gamma}$ distinguishes different scattering mechanisms. For example, $\gamma = 1$ is for e-ph interaction and $\gamma = 0.5$ is for e-e interaction [20,22]. The Fig. 5(b) inset presents gate-dependent γ extracted from the power-law fitting of L_ϕ . Measured values of γ are close to 0.5 in all gate ranges which is in good agreement with AAK theory described in Eq. (2). The slight deviation from 0.5 can be explained by the temperature dependence of σ_{xx} . By plotting experimentally extracted L_ϕ as a function of conductance σ_{xx} [Fig. 5(c)], we can confirm that the near-linear dependence between gate voltage and phase-coherence length at fixed temperatures originates from electron-electron interaction. Therefore, we conclude that electron-electron interaction is the main phase-relaxation mechanism in Te within temperatures ranging from 1 to 18 K.

Interestingly, quantum interference effects, such as WL and WAL, are sensitive to the relative strength of spin relaxation and phase coherence as we discussed before. The system shows WAL when the phase-coherence length is larger than the spin-relaxation length and WL otherwise [43]. The gate-dependent transition from WAL to WL is observed at a higher temperature (18 K) [Fig. 5(d)]. According to the AAK theory [Eq. (2)], the phase-coherence length L_ϕ is small in the region of high temperatures and low gate voltage (low longitudinal

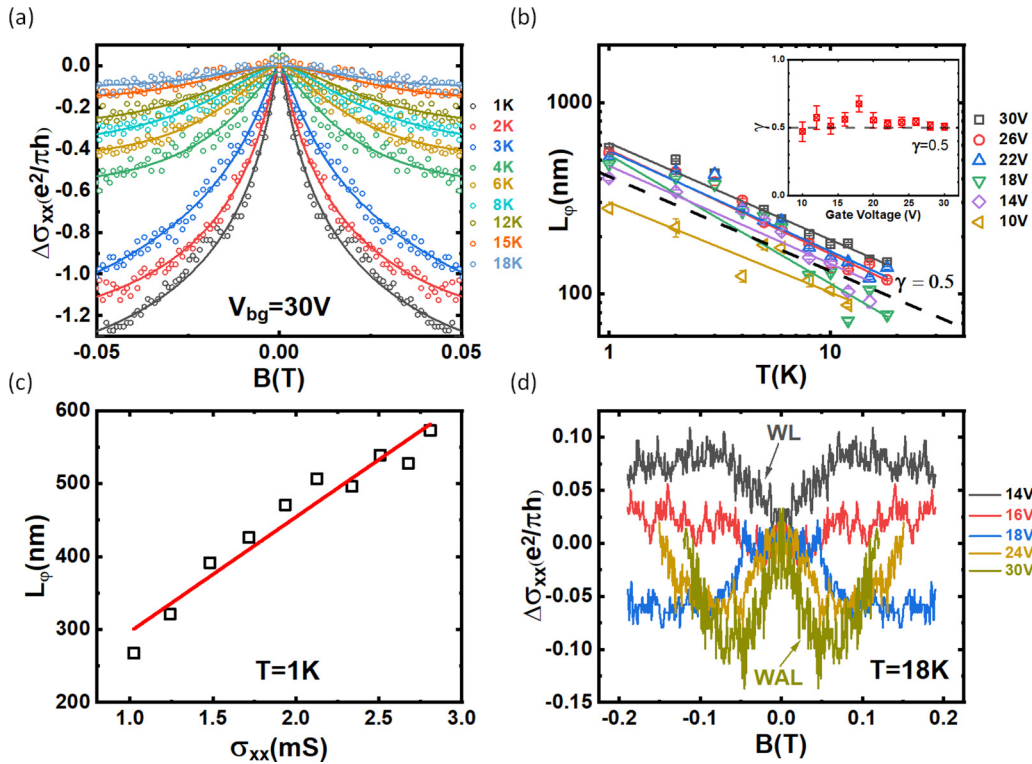


FIG. 5. Temperature dependence of WAL. (a) Theoretical fits (solid lines) with ILP theory to temperature-dependent experimental data (circles) measured at $V_{bg} = 30$ V. Zero-field conductivity is calculated ($\sigma_{xx} = 226.6\text{--}227.9 e^2/\pi h$). (b) Temperature-dependent phase-coherence length L_ϕ (data points) extracted from WAL at different gate-voltage fits with a power law (solid lines) in a log-log plot (black dashed line is $\Upsilon = 0.5$). The inset: Gate-dependent coefficient Υ extracted from the power-law fitting is close to 0.5 in all gate voltages which indicates the electron-electron interaction is responsible for the dephasing process. (c) Phase-coherence length L_ϕ as a function of the sheet conductance σ_{xx} at $T = 1$ K. The red line is the linear fitting of L_ϕ and σ_{xx} . (d) Transition from WL to WAL at $T = 18$ K. Zero-field conductivity is calculated ($\sigma_{xx} = 104.8\text{--}226.6 e^2/\pi h$).

conductance σ_{xx}). In the meantime, spin-relaxation length L_{so} decreases with gate voltage [Fig. 3(d)] because of the Rashba and Dresselhaus SOIs. Therefore, WL is observed when the phase-coherence length is $L_\phi < L_{so}$ at $V_{bg} = 14$ V. With the increase in gate voltage, WAL emerges under the condition of $L_\phi > L_{so}$ at $V_{bg} > 18$ V.

In conclusion, gate-tunable strong spin-orbit interaction-induced WAL has been observed in 2D n -type Te films. Gate- and temperature-dependent WALs are systematically measured and analyzed. We find that the k -linear spin-precession vector is much smaller than the k -cubic spin-precession vector by fitting experimental data with ILP theory. Large phase-coherence length near 600 nm together with gate-tunable SOI make n -type 2D Te films a competitive candidate for spintronic applications. Furthermore, we determine that the DP spin-relaxation mechanism is dominant and the electron-electron interaction with a small energy

transfer is the main mechanism for inelastic scattering at low temperatures for 2D Te films.

P.D.Y. was supported by the NSF/AFOSR 2DARE Program, the ARO, and the SRC. W.W. acknowledges the College of Engineering and School of Industrial Engineering at Purdue University for startup support. W.W. was partially supported by a Grant from the Oak Ridge Associated Universities (ORAU) Junior Faculty Enhancement Award Program. A portion of this work was performed at the National High Magnetic Field Laboratory, which was supported by the National Science Foundation Cooperative Agreement No. DMR-1644779 and the State of Florida. C.N. acknowledges valuable discussions with J. Li and X. Wang. C.N. and G.Q. acknowledge technical support from National High Magnetic Field Laboratory (NHMFL) staffs J. Jaroszynski, A. Suslov, and W. Coniglio.

- [1] K. F. Mak, K. L. McGill, J. Park, and P. L. McEuen, *Science* **344**, 1489 (2014).
 [2] Z. Wu, B. T. Zhou, X. Cai, P. Cheung, G. Bin Liu, M. Huang, J. Lin, T. Han, L. An, Y. Wang, S. Xu, G. Long, C. Cheng, K. T. Law, F. Zhang, and N. Wang, *Nat. Commun.* **10**, 611 (2019).
 [3] S. Xu, J. Shen, G. Long, Z. Wu, Z. Q. Bao, C. C. Liu, X. Xiao, T. Han, J. Lin, Y. Wu, H. Lu, J. Hou, L. An, Y. Wang, Y. Cai,

- K. M. Ho, Y. He, R. Lortz, F. Zhang, and N. Wang, *Phys. Rev. Lett.* **118**, 067702 (2017).
 [4] H. C. P. Movva, B. Fallahazad, K. Kim, S. Larentis, T. Taniguchi, K. Watanabe, S. K. Banerjee, and E. Tutuc, *Phys. Rev. Lett.* **118**, 247701 (2017).
 [5] T. S. Ghiasi, J. Ingla-Ayne, A. A. Kaverzin, and B. J. van Wees, *Nano Lett.* **17**, 7528 (2017).

- [6] J. O. Island, X. Cui, C. Lewandowski, J. Y. Khoo, E. M. Spanton, H. Zhou, D. Rhodes, J. C. Hone, T. Taniguchi, K. Watanabe, L. S. Levitov, M. P. Zaletel, and A. F. Young, *Nature (London)* **571**, 85 (2019).
- [7] J. Nitta, T. Akazaki, H. Takayanagi, and T. Enoki, *Phys. Rev. Lett.* **78**, 1335 (1997).
- [8] T. Koga, J. Nitta, T. Akazaki, and H. Takayanagi, *Phys. Rev. Lett.* **89**, 046801 (2002).
- [9] W. Knap, C. Skierbiszewski, A. Zduniak, E. Litwin-Staszewska, D. Bertho, F. Kobbi, J. Robert, and G. Pikus, *Phys. Rev. B* **53**, 3912 (1996).
- [10] G. Chang, B. J. Wieder, F. Schindler, D. S. Sanchez, I. Belopolski, S. M. Huang, B. Singh, D. Wu, T. R. Chang, T. Neupert, S. Y. Xu, H. Lin, and M. Z. Hasan, *Nature Mater.* **17**, 978 (2018).
- [11] G. L. Chen, J. Han, T. T. Huang, S. Datta, and D. B. Janes, *Phys. Rev. B* **47**, 4084 (1993).
- [12] S. V. Morozov, K. S. Novoselov, M. I. Katsnelson, F. Schedin, L. A. Ponomarenko, D. Jiang, and A. K. Geim, *Phys. Rev. Lett.* **97**, 016801 (2006).
- [13] R. V. Gorbachev, F. V. Tikhonenko, A. S. Mayorov, D. W. Horsell, and A. K. Savchenko, *Phys. Rev. Lett.* **98**, 176805 (2007).
- [14] A. T. Neal, H. Liu, J. Gu, and P. D. Ye, *ACS Nano* **7**, 7077 (2013).
- [15] H. Schmidt, I. Yudhistira, L. Chu, A. H. Castro Neto, B. Özyilmaz, S. Adam, and G. Eda, *Phys. Rev. Lett.* **116**, 046803 (2016).
- [16] Y. Du, A. T. Neal, H. Zhou, and P. D. Ye, *J. Phys. Condens. Matter* **28**, 263002 (2016).
- [17] Y. Shi, N. Gillgren, T. Espiritu, S. Tran, J. Yang, K. Watanabe, T. Taniguchi, and C. N. Lau, *2D Materials* **3**, 3 (2016).
- [18] G. Long, S. Xu, X. Cai, Z. Wu, T. Han, J. Lin, C. Cheng, Y. Cai, X. Wang, and N. Wang, *Nanotechnology* **29**, 035204 (2018).
- [19] N. Hemsforth, V. Tayari, F. Telesio, S. Xiang, S. Roddaro, M. Caporali, A. Ienco, M. Serrano-Ruiz, M. Peruzzini, G. Gervais, T. Szkopek, and S. Heun, *Phys. Rev. B* **94**, 245404 (2016).
- [20] J. Hu, X. Liu, C. L. Yue, J. Y. Liu, H. W. Zhu, J. B. He, J. Wei, Z. Q. Mao, L. Yu Antipina, Z. I. Popov, P. B. Sorokin, T. J. Liu, P. W. Adams, S. M. A Radmanesh, L. Spinu, and H. Ji, *Nat. Phys.* **11**, 471 (2015).
- [21] S. Takasuna, J. Shiogai, S. Matsuzaka, M. Kohda, Y. Oyama, and J. Nitta, *Phys. Rev. B* **96**, 161303(R) (2017).
- [22] J. Zeng, S. J. Liang, A. Gao, Y. Wang, C. Pan, C. Wu, E. Liu, L. Zhang, T. Cao, X. Liu, Y. Fu, Y. Wang, K. Watanabe, T. Taniguchi, H. Lu, and F. Miao, *Phys. Rev. B* **98**, 125414 (2018).
- [23] A. T. Neal, Y. Du, H. Liu, and P. D. Ye, *ACS Nano* **8**, 9137 (2014).
- [24] H. T. He, G. Wang, T. Zhang, I. K. Sou, G. K. L. Wong, J. N. Wang, H. Z. Lu, S. Q. Shen, and F. C. Zhang, *Phys. Rev. Lett.* **106**, 166805 (2011).
- [25] J. Chen, H. J. Qin, F. Yang, J. Liu, T. Guan, F. M. Qu, G. H. Zhang, J. R. Shi, X. C. Xie, C. L. Yang, K. H. Wu, Y. Q. Li, and L. Lu, *Phys. Rev. Lett.* **105**, 176602 (2010).
- [26] B. Zhao, P. Cheng, H. Pan, S. Zhang, B. Wang, G. Wang, F. Xiu, and F. Song, *Sci. Rep.* **6**, 22377 (2016).
- [27] H. Z. Lu and S. Q. Shen, *Phys. Rev. B* **92**, 035203 (2015).
- [28] L. A. Agapito, N. Kioussis, W. A. Goddard, and N. P. Ong, *Phys. Rev. Lett.* **110**, 176401 (2013).
- [29] M. Hirayama, R. Okugawa, S. Ishibashi, S. Murakami, and T. Miyake, *Phys. Rev. Lett.* **114**, 206401 (2015).
- [30] V. A. Berezovets, I. I. Farbshtein, and A. L. Shelankov, *JETP Lett.* **39**, 2 (1984).
- [31] G. Qiu, S. Huang, M. Segovia, P. K. Venuthurumilli, Y. Wang, W. Wu, X. Xu, and P. D. Ye, *Nano Lett.* **19**, 1955 (2019).
- [32] G. Qiu, Y. Wang, Y. Nie, Y. Zheng, K. Cho, W. Wu, and P. D. Ye, *Nano Lett.* **18**, 5760 (2018).
- [33] K. Nakayama, M. Kuno, K. Yamauchi, S. Souma, K. Sugawara, T. Oguchi, T. Sato, and T. Takahashi, *Phys. Rev. B* **95**, 125204 (2017).
- [34] G. Qiu, C. Niu, Y. Wang, M. Si, Z. Zhang, W. Wu, and P. D. Ye, *arXiv:1908.11495*.
- [35] Y. Du, G. Qiu, Y. Wang, M. Si, X. Xu, W. Wu, and P. D. Ye, *Nano Lett.* **17**, 3965 (2017).
- [36] S. Berweger, G. Qiu, Y. Wang, B. Pollard, K. L. Genter, R. Tyrrell-Ead, T. M. Wallis, W. Wu, P. D. Ye, and P. Kabos, *Nano Lett.* **19**, 1289 (2019).
- [37] G. Qiu, M. Si, Y. Wang, X. Lyu, W. Wu, and P. D. Ye, *2018 76th Device Research Conference (DRC)* (IEEE, Santa Barbara, CA, 2018).
- [38] H. Liu, A. T. Neal, M. Si, Y. Du, and P. D. Ye, *IEEE Electron Device Lett.* **35**, 795 (2014).
- [39] A. Prakash, Y. Cai, G. Zhang, Y. W. Zhang, and K. W. Ang, *Small* **13**, 1602909 (2017).
- [40] See Supplemental Material at <http://link.aps.org/supplemental/10.1103/PhysRevB.101.205414> for the extraction of effective mass, the detail of WAL fitting, and WAL in *p*-type 2D Te.
- [41] M. I. Dyakonov and V. I. Perel, *Phys. Lett. A* **35**, 459 (1971).
- [42] A. Manchon, H. C. Koo, J. Nitta, S. M. Frolov, and R. A. Duine, *Nature Mater.* **14**, 871 (2015).
- [43] H. Yuan, M. Saeed Bahramy, and B.-J. Yang, *Nat. Phys.* **9**, 563 (2013).
- [44] E. I. Rashba, *Soviet Phys. Solid State* **2**, 1109 (1960).
- [45] G. Dresselhaus, *Phys. Rev.* **98**, 368 (1955).
- [46] H. Nakamura, T. Koga, and T. Kimura, *Phys. Rev. Lett.* **108**, 206601 (2012).
- [47] S. Hikami, A. I. Larkin, and Y. Nagaoka, *Prog. Theor. Phys.* **63**, 707 (1980).
- [48] S. V. Iordanskii, Y. B. Lyanda-Geller, and G. E. Pikus, *JETP Lett.* **60**, 206 (1994) [*Pis' ma Zh. Eksp. Teor. Fiz.* **60**, 199 (1994)].
- [49] G. M. Minkov, A. V. Germanenko, and I. V. Gornyi, *Phys. Rev. B* **70**, 245423 (2004).
- [50] H. Shinno, R. Yoshizaki, S. Tanaka, T. Doi, and H. Kamimura, *J. Phys. Soc. Jpn.* **35**, 525 (1973).
- [51] X. Ren, Y. Wang, Z. Xie, F. Xue, C. Leighton, and C. Daniel Frisbie, *Nano Lett.* **19**, 4738 (2019).
- [52] H. Liu, L. Bao, Z. Zhou, B. Che, R. Zhang, C. Bian, R. Ma, L. Wu, H. Yang, J. Li, C. Gu, C. - M. Shen, S. Du, and H. - J. Gao, *Nano Lett.* **19**, 4551 (2019).
- [53] Q. Wang, P. Yu, X. Huang, J. Fan, X. Jing, Z. Ji, Z. Liu, G. Liu, C. Yang, and L. Lu, *Chin. Phys. Lett.* **35**, 077303 (2018).
- [54] P. Song, C. Hsu, M. Zhao, X. Zhao, T. Chang, J. Teng, H. Lin, and K. P. Loh, *2D Mater.* **5**, 031010 (2018).
- [55] B. L. Altshuler, A. G. Aronov, and D. E. Khmel'nitsky, *J. Phys. C: Solid State Phys.* **15**, 7367 (1982).